Direct simulation of isothermal-wall supersonic channel flow

By Gary N. Coleman

1. Motivation, objectives, and approach

The motivation for this work is the fact that in turbulent flows where compressibility effects are important, they are often poorly understood. A few examples of such flows are those associated with astrophysical phenomena and those found in combustion chambers, supersonic diffusers and nozzles, and over high-speed airfoils. For this project, we are primarily interested in compressibility effects near solid surfaces. Our main objective is an improved understanding of the fundamentals of compressible wall-bounded turbulence, which can in turn be used to cast light upon modeling concepts such as the Morkovin hypothesis and the Van Driest transformation (Bradshaw 1977).

To this end, we have performed a direct numerical simulation (DNS) study of supersonic turbulent flow in a plane channel with constant-temperature walls. All of the relevant spatial and temporal scales are resolved so that no subgrid scale or turbulence model is necessary. The channel geometry was chosen so that finite Mach number effects can be isolated by comparing the present results to well-established incompressible channel data (Kim, Moin & Moser 1987). Here the fluid is assumed to be an ideal gas with constant specific heats, constant Prandtl number, and power-law temperature-dependent viscosity. Isothermal-wall boundary conditions are imposed so that a statistically stationary state may be obtained. The flow is driven by a uniform (in space) body force (rather than a mean pressure gradient) to preserve streamwise homogeneity, with the body force defined so that the total mass flux is constant.

The variables are nondimensionalized by the wall temperature, the channel half-width, the bulk-averaged ("mixed-mean") density, and the bulk velocity, such that $\frac{1}{2}\int_{-1}^{+1}\overline{\rho}dy = 1$ and $\frac{1}{2}\int_{-1}^{+1}\overline{\rho u}dy = 1$, where the channel walls are at $y = \pm 1$. All variables are henceforth assumed to be dimensionless, with ρ representing the density, $u = u_1$ the streamwise velocity, $(x, y, z) = (x_1, x_2, x_3)$ respectively the streamwise, wall-normal, and spanwise coordinates, and an overbar defines an average over time and streamwise and spanwise directions. The nondimensional governing equations are:

$$\frac{\partial \rho}{\partial t} + u_j \frac{\partial \rho}{\partial x_j} = -\rho \frac{\partial u_j}{\partial x_j}, \tag{1}$$

$$\frac{\partial u_i}{\partial t} + u_j \frac{\partial u_i}{\partial x_j} = -\frac{1}{\gamma M^2}\frac{\partial T}{\partial x_i} - \frac{T}{\gamma M^2 \rho}\frac{\partial \rho}{\partial x_i} + \frac{1}{Re}\frac{1}{\rho}\frac{\partial \tau_{ij}}{\partial x_j} + \Phi_i, \tag{2}$$

$$\frac{\partial T}{\partial t} + u_j \frac{\partial T}{\partial x_j} = -(\gamma - 1)T\frac{\partial u_j}{\partial x_j} + \frac{\gamma(\gamma-1)M^2}{Re}\frac{\tau_{ij}}{\rho}\frac{\partial u_i}{\partial x_j} - \frac{\gamma}{Re\ Pr}\frac{1}{\rho}\frac{\partial q_j}{\partial x_j} + \mathcal{S}, \tag{3}$$

where

$$\tau_{ij} = \mu\left(\frac{\partial u_i}{\partial x_j} + \frac{\partial u_j}{\partial x_i} - \frac{2}{3}\delta_{ij}\frac{\partial u_l}{\partial x_l}\right) \quad \text{and} \quad q_j = -\mu\frac{\partial T}{\partial x_j}.$$

The pressure is normalized by the bulk density and bulk velocity, so the ideal gas law is $p = \rho T/\gamma M^2$. The body force term Φ_i is nonzero only for $i = 1$. The purpose of $\mathcal{S}$, the source/sink term in (3), is explained below. Equations (1) - (3) are to be solved numerically subject to the isothermal, no-slip boundary conditions,

$$T = 1 \quad \text{and} \quad \mathbf{u} = 0 \quad \text{at} \quad y = \pm 1. \tag{4}$$

We therefore have as relevant nondimensional parameters (*i*) a Mach number, M, based on the bulk velocity and wall sound speed; (*ii*) a Reynolds number, Re, based on the bulk density, bulk velocity, channel halfwidth, and wall viscosity; (*iii*) the Prandtl number, Pr; (*iv*) the ratio of specific heats, γ; and (*v*) the viscosity exponent, n, where the dynamic viscosity $\mu \propto T^n$. These 5 parameters are used to define the various DNS runs. But besides choosing appropriate values for the "physical" parameters, we will also artificially introduce another - to allow us to differentiate between mean and fluctuation compressibility effects.

The Mach number appears in the energy equation (3) in the term that represents the irreversible loss of kinetic energy into heat. Following Buell (1991), we interpret (in our simulations) the actual Mach number M in (2) and the "dissipation Mach number" M_d in (3) as separate parameters. By setting M_d to values different from M in the DNS, we produce an effective heat source/sink $\mathcal{S}$ in (3) which is given by

$$\mathcal{S} = (M_d^2 - M^2)\,\frac{\gamma(\gamma-1)}{Re}\,\frac{\tau_{ij}}{\rho}\,\frac{\partial u_i}{\partial x_j}. \tag{5}$$

Consequently, we can consider cases with different mean temperature profiles (and thus different mean property variations) at the same M. Results from these "unphysical" $M \neq M_d$ DNS runs can, therefore, be used to determine the relative importance of turbulent-fluctuation and variable-property influences at a given Mach number.

Three DNS cases will be discussed, with the Mach number ranging from $M = 1.5$ to 3. All the runs share the same Prandtl number, specific heat ratio, and viscosity exponent ($Pr = 0.7$, $\gamma = 1.4$ and $n = 0.7$), while the Reynolds number (for reasons given below) is either 3000 or 4880. A summary of the parameters is listed in table 1. Cases denoted by a single letter (A and B) in table 1 represent "physical" simulations for which $M_d = M$. For the $M_d \neq M$ run, Case AX, $M = 1.5$ and $M_d = 0$. Since the temperature fields in both the physical and unphysical runs depend almost exclusively on M_d (Coleman *et al.* 1993), this parameter combination will produce the behavior of the "extra" source/sink $\mathcal{S}$, eq. (5), that is necessary to isolate mean and fluctuation effects. With $M_d = 0$, $\mathcal{S}$ is such that the mean temperature and density are constant across the channel, as we shall see below.

The DNS results were generated using the code developed by Buell to study compressible Couette flow. During the computations, the body force Φ_i is adjusted

Table 1. DNS physical parameters.

Case	M	M_d	Re	Pr	γ	μ
A	1.5	1.5	3000	0.7	1.4	$T^{0.7}$
B	3	3	4880	0.7	1.4	$T^{0.7}$
AX	1.5	0	3000	0.7	1.4	$T^{0.7}$

Table 2. DNS numerical parameters.

nx	ny	nz	nxc	nyc	nzc	L_x	L_z
110	90	60	144	119	80	4π	$4\pi/3$

so that the total mass flux through the channel remains constant. (Once the flow reaches a statistically stationary state the variations of Φ_i with time are small). The code utilizes a Fourier-Legendre spectral discretization along with a hybrid implicit-explicit third-order time-advance algorithm designed to maximize the range of Mach numbers that may be considered (Buell 1991). The numerical parameters used by all three runs are given in table 2, where L_x and L_z are the streamwise and spanwise domain sizes, and (nx, ny, nz) and (nxc, nyc, nzc) are respectively the number of expansion coefficients and collocation (quadrature) points in the streamwise, wall-normal, and spanwise directions. The runs were made on the CCF and NAS Cray YMP and C-90 computers at NASA Ames Research Center.

2. Results

An indication of the numerical fidelity of the DNS is provided by the streamwise and spanwise one-dimensional spectra from the channel centerline and near the walls, shown in figure 1. They are typical of those found from all three DNS runs in their rapid fall-off at high wavenumber, which implies that the x- and z-resolution is adequate. The "Legendre spectra" (not shown) also verify that the wall-normal resolution is sufficient. The high wavenumber streamwise and spanwise spectra of the velocity at both the channel centerline (figure 1(a,b)) and near the wall (figure 1(c,d)) are similar to those found in the incompressible channel (see figure 3 of Kim *et al.* 1987). In the present simulations, we find that the density and temperature spectra are closely related to each other and that their magnitudes are much larger near the walls than they are at the centerline. The streamwise and spanwise correlations in figure 2 are also roughly equivalent to the incompressible results (cf. figure 2 of Kim *et al.* 1987) except for two characteristics: the large spanwise coherence of the density and temperature at the centerline (figure 2b), and the greater streamwise coherence of the ρ, u, and T fields near the wall (figure 2c).

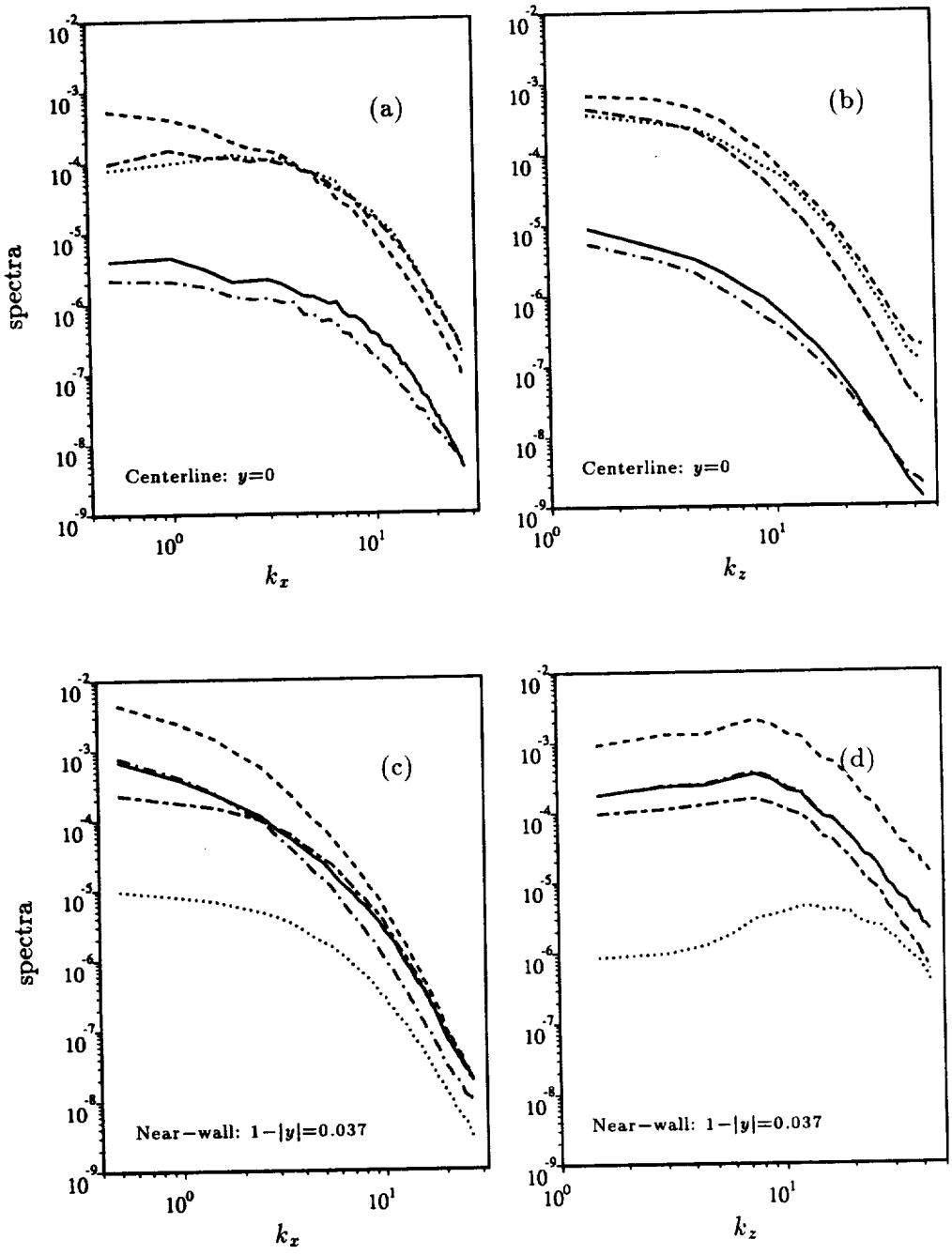

FIGURE 1. One-dimensional spectra for Case A: ——, ρ; - - - -, u; ·····, v; — — —, w; —·—, T. (a) & (c) Streamwise; (b) & (d) spanwise.

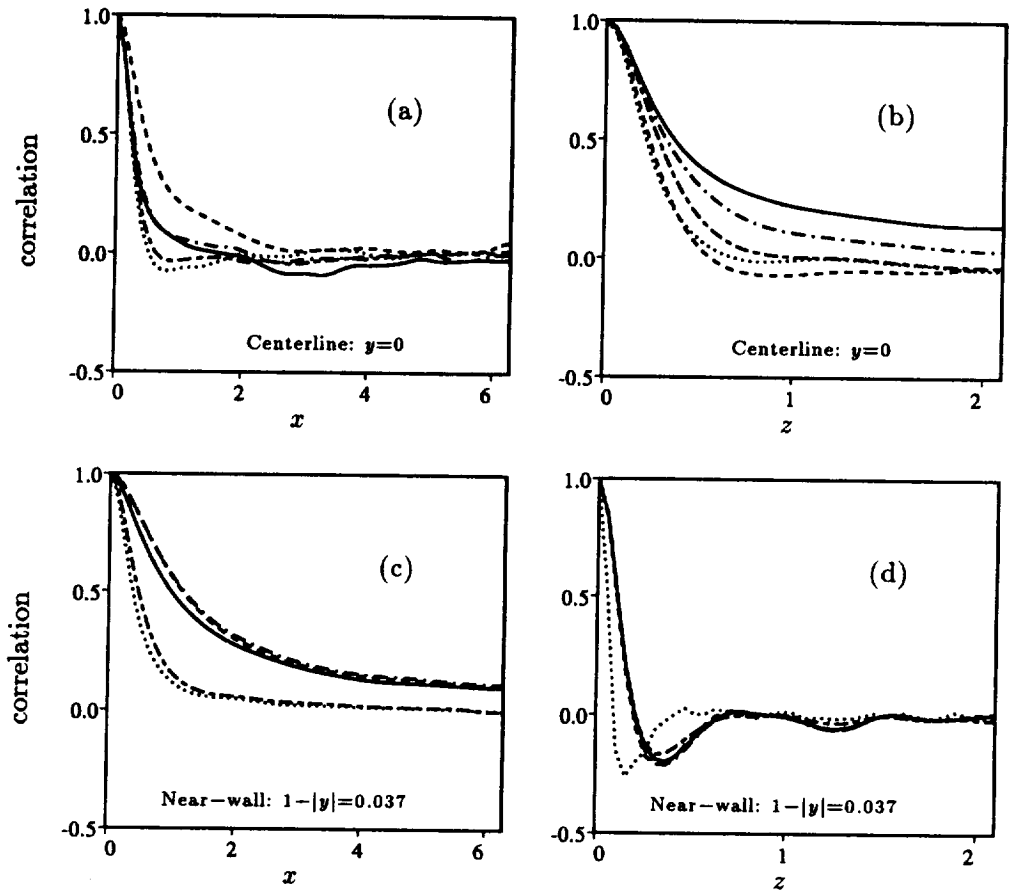

FIGURE 2. Two-point correlations for Case A: symbols as in figure 1. (a) & (c) Streamwise; (b) & (d) spanwise.

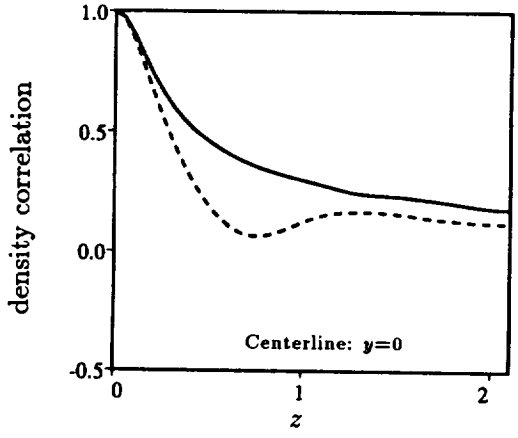

FIGURE 3. Two-point density correlations for Case A at channel centerline: ——, full field; ----, with acoustic eigenfunctions removed.

We first discuss the spanwise coherence at the centerline, which is thought to be due to acoustic resonance. Evidence for this is provided first by the fact that the coherence is not present in the velocity, and most significantly by the results in figure 3, which contrast the spanwise density correlation from an instantaneous field (one which contributed to the figure 2b curve) with that obtained by eliminating the contribution from several "acoustic eigenfunctions." This is done by projecting the DNS fields on eigenfunctions of the linear inviscid isentropic problem for a given base flow. The acoustic density and velocity fluctuations are respectively assumed to satisfy $\rho^{\mathrm{a}}(\mathbf{x},t) = \sum_{\mathbf{k}} \widehat{\rho}(\mathbf{k},y)\mathrm{e}^{\mathrm{i}(\mathbf{k}\cdot\mathbf{x}-\omega t)}$ and $u_{\mathrm{i}}^{\mathrm{a}}(\mathbf{x},t) = \sum_{\mathbf{k}} \widehat{u}_{\mathrm{i}}(\mathbf{k},y)\mathrm{e}^{\mathrm{i}(\mathbf{k}\cdot\mathbf{x}-\omega t)}$. At a given wavenumber $\mathbf{k} = (k_x, k_z)$, the linearized, isentropic Euler equations in Fourier space in terms of the "acoustic eigenfunctions" $\mathbf{q}_\ell(\mathbf{k},y) = (\widehat{\rho}(\mathbf{k},y), \widehat{u}(\mathbf{k},y), \widehat{v}(\mathbf{k},y), \widehat{w}(\mathbf{k},y))_\ell^T$ can then be written as $\mathcal{L}(\mathbf{q}) = \omega\mathbf{q}$, where

$$\mathcal{L}(\mathbf{q}) = \begin{pmatrix} k_x\overline{u}\widehat{\rho} + k_x\overline{\rho}\widehat{u} - \mathrm{i}(\overline{\rho}\widehat{v})_y + k_z\overline{\rho}\widehat{w} \\ k_x\overline{u}\widehat{u} - \mathrm{i}(d\overline{u}/dy)\widehat{v} + k_x\frac{\mathrm{a}^2}{\overline{\rho}}\widehat{\rho} \\ k_x\overline{u}\widehat{v} - \mathrm{i}\mathrm{a}^2(\widehat{\rho}/\overline{\rho})_y \\ k_x\overline{u}\widehat{w} + k_z\frac{\mathrm{a}^2}{\overline{\rho}}\widehat{\rho} \end{pmatrix}, \tag{6}$$

with a equal to the sound speed and $\widehat{v} = 0$ at $y = \pm 1$.

The projection of the full DNS field onto the acoustic subspace is performed by computing the inner product $\int_{-1}^{+1} \mathbf{q}_{\mathrm{DNS}} \cdot \mathbf{q}_m^\star dy$ of the DNS field with eigenfunctions $\mathbf{q}_m^\star$ of the adjoint problem to (6), $\mathcal{L}^\star(\mathbf{q}^\star) = \omega\mathbf{q}^\star$, such that $\int_{-1}^{+1} \mathcal{L}(\mathbf{q}) \cdot \mathbf{q}^\star dy \equiv \int_{-1}^{+1} \mathbf{q} \cdot \mathcal{L}^\star(\mathbf{q}^\star) dy$. The adjoint operator is

$$\mathcal{L}^\star(\mathbf{q}^\star) = \begin{pmatrix} k_x\overline{u}\widehat{\rho}_\star + k_x\frac{\mathrm{a}^2}{\overline{\rho}}\widehat{u}_\star + \frac{\mathrm{i}}{\overline{\rho}}(\mathrm{a}^2\widehat{v}_\star)_y + k_z\frac{\mathrm{a}^2}{\overline{\rho}}\widehat{w}_\star \\ k_x\overline{u}\widehat{u}_\star + k_x\overline{\rho}\widehat{\rho}_\star \\ k_x\overline{u}\widehat{v}_\star + \mathrm{i}\overline{\rho}(\widehat{\rho}_\star)_y - \mathrm{i}(d\overline{u}/dy)\widehat{u}_\star \\ k_x\overline{u}\widehat{w}_\star + k_z\overline{\rho}\widehat{\rho}_\star \end{pmatrix}, \tag{7}$$

where $\widehat{v}_\star = 0$ at $y = \pm 1$.

When the base flow is uniform (no y variation), the eigenfunctions from (6) are irrotational, and the eigenvalues ω from (6) and (7) give phase speeds $c_x = \mathrm{Real}(\omega)/k_x$ that satisfy

$$\overline{u} - c_x = \pm\mathrm{a}[(\ell\pi/2k_x)^2 + 1]^{1/2}, \tag{8}$$

where ℓ is the wall-normal wave number (equivalent to the number of times $|\widehat{\rho}|$ and $|\widehat{u}|$ change sign between $-1 \le y \le +1$). Here we use the Case A mean profiles shown in figure 4 as the base flow and numerically compute solutions to (6) and (7), which leads to "acoustic" (isentropic) eigenfunctions that do not satisfy the above phase relation and, in fact, have nonzero vorticity near the walls. Near the channel centerline, however, the eigenfunctions have a more typically acoustic behavior in that their ratio of dilation to enstrophy is very large and in that a given ℓ mode (now

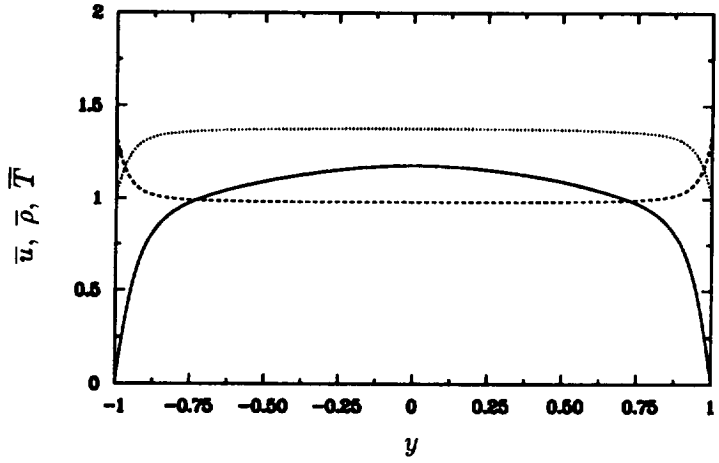

FIGURE 4. Mean profiles for Case A: ——, $\overline{u}$; ----, $\overline{\rho}$; ····· , $\overline{T}$.

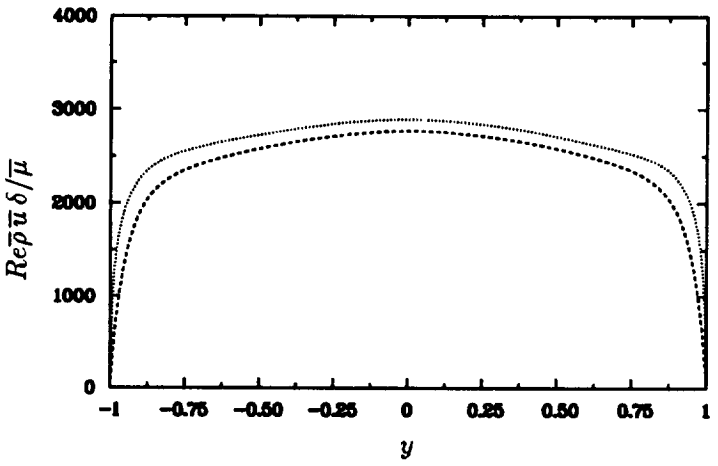

FIGURE 5. Local Reynolds number profiles: ----, Case A; ····· , Case B.

defined as the number of $|\widehat{\rho}|$ sign changes) consists of an upstream- and downstream-propagating pair† with positive and negative phase speeds relative to the centerline velocity, $\overline{u}_c - c_x$. The dashed curve in figure 3 represents the density field after the isentropic modes $\mathbf{q}_\ell$ that are recognized as acoustic in the range $\ell = [0, \ldots, 4]$ have been projected and removed, for $k_x L_x/2\pi = [0, \ldots, +4]$ (using conjugate symmetry to account for $k_x < 0$) and $k_z L_z/2\pi = [-4, \ldots, +4]$. Only the eigenfunctions with (a) very large dilation-to-enstrophy ratio near the centerline, (b) an equal number of sign changes for $|\widehat{\rho}|$ and for $|\widehat{u}|$, and (c) no more than two modes at each ℓ – one with positive and one with negative relative phase speed – were chosen from the full inviscid isentropic function space to be included in the projection. The second criterion is overly conservative: it is useful when automating the selection

† Although some ℓ modes appear to have only a single downstream-propagating component.

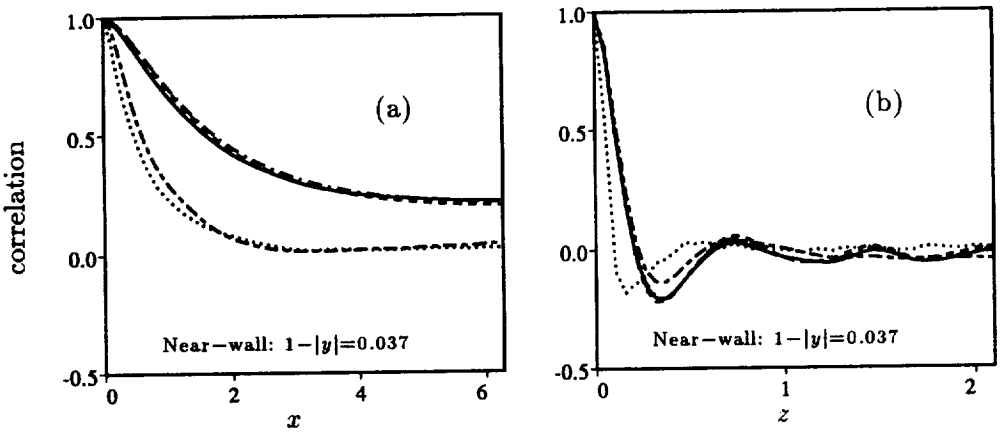

FIGURE 6. Near-wall two-point correlations for Case B: symbols as in figure 1. (a) Streamwise; (b) spanwise.

process, but excludes a few modes (because of low amplitude "wiggles" in $|\widehat{u}|$) that are thought to be acoustic rather than vortical. For this reason, and perhaps also because of physical differences between the uniform and variable mean cases that produce at certain ℓ no non-vortical modes moving upstream with respect to the centerline velocity, the projection at some $\mathbf{k}$ did not include two modes for every ℓ in the 0 to 4 range. Nevertheless, the magnitude of the reduction in figure 3 suggests that there are significant acoustic disturbances within the simulation results. The correlation at $z \approx 2$ would presumably be reduced still further if more $k_z = 0$ modes were used in the projection. Note that because the computations assume that the channel walls are perfectly rigid (and use periodic boundary conditions), any acoustic signals present in the DNS are not necessarily expected to be identical to those found in a laboratory wind tunnel since in the simulations there is no mechanism for the acoustic energy to radiate away.

The other difference, mentioned above, between the two-point correlations for the present and incompressible DNS is in the larger near-wall streamwise correlations found in figure 2c; this indicates that the near-wall streaks, which are characteristic of wall-bounded turbulent flows (Robinson 1991), are more coherent in Case A than in the incompressible channel results. At first glance, it might appear that the streak modification is a low Reynolds number effect (so that the effective streamwise domain size in wall units is smaller) since the Reynolds number based on mean centerline velocity is higher in the incompressible DNS than that found here. The variation of the local Reynolds number across the channel is shown by the dashed curve in figure 5, and the centerline value (2770) is seen to be slightly less than the 3300 quoted for the incompressible channel data (Kim *et al.* 1987). But because the isothermal boundary conditions lead to a flow with a maximum mean temperature near the centerline and maximum density at the walls (figure 4), the mean kinematic viscosity $\overline{\mu}/\overline{\rho}$ (where $\overline{\mu} = \overline{T}^n$) is maximum at $y = 0$. Therefore, the local Reynolds

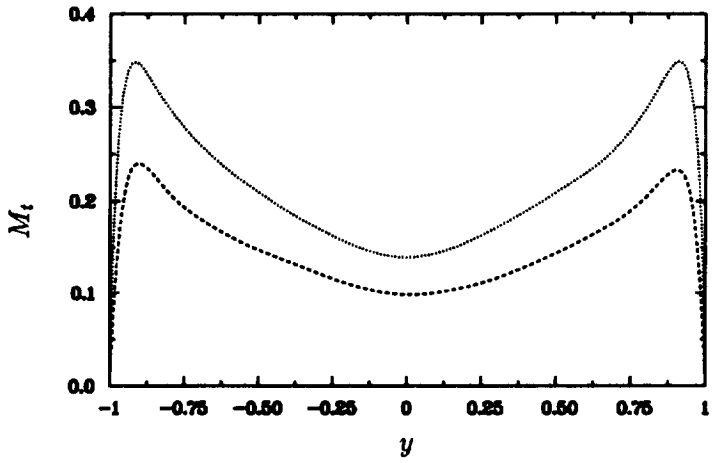

FIGURE 7. Turbulent Mach number, $M_t = M\sqrt{\overline{u_i'u_i'}}/\sqrt{\overline{T}}$: ----, Case A; ·····, Case B.

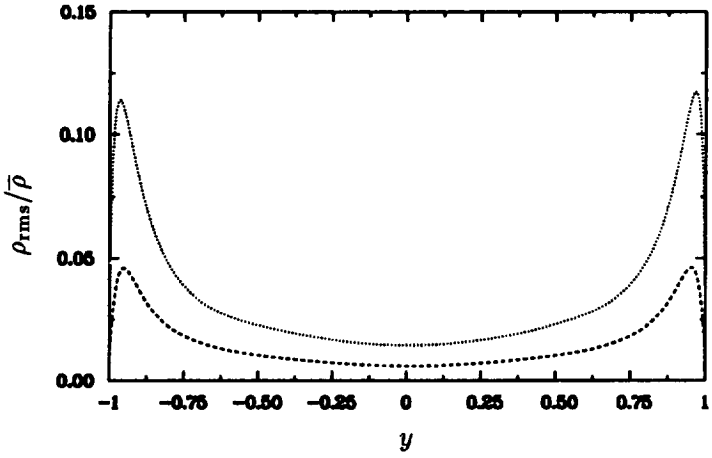

FIGURE 8. Root mean square density fluctuations: ----, Case A; ·····, Case B.

number in the present DNS is apt to be larger near the walls than for when $\nu =$ constant. This suggests that the enhanced near-wall coherence in figure 2c is solely a compressibility effect, a fact that is reinforced by the Case B results. In order to obtain a local Reynolds number profile $Re\overline{\rho}\,\overline{u}\,\delta/\overline{\mu}$ (where $\delta = 1$) at $M = 3$ (Case B) that remains comparable to that for Case A, the bulk Reynolds number was increased from 3000 to 4880. As the Case B profile (dotted curve) in figure 5 shows, the Reynolds number is in fact at any y slightly larger than that for Case A (dashed), which implies that the further increase shown in figure 6a (over that seen in figure 2c) of the near-wall streamwise correlation for Case B is not a viscous effect.

It therefore appears that the extra coherence is due to compressibility, although its precise source is at this point uncertain. One possibility is near-wall viscosity

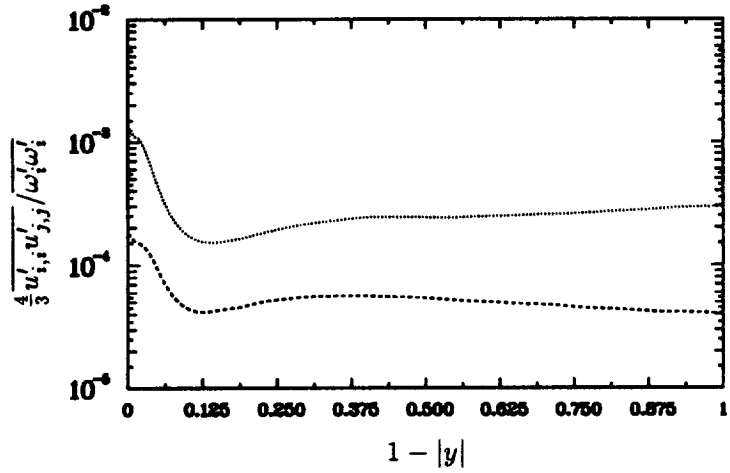

FIGURE 9. Dilatation-to-enstrophy ratio: ----, Case A; ····· , Case B.

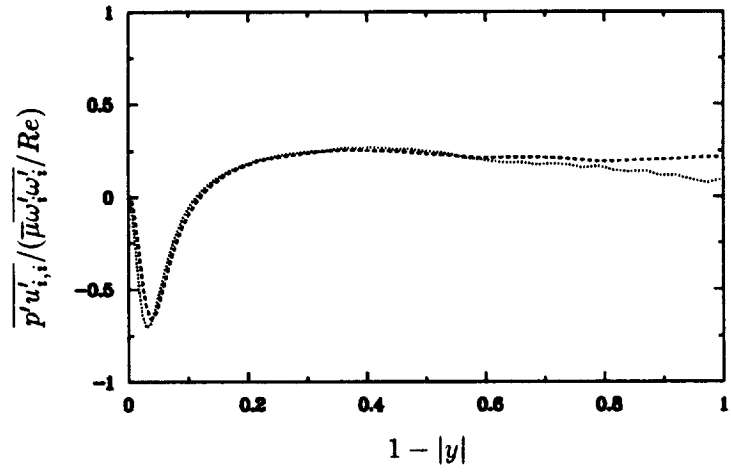

FIGURE 10. Pressure-dilatation correlation: ----, Case A; ····· , Case B.

fluctuations (Tritton 1961; Bradshaw & Ferriss 1971); another is small-scale acoustic fluctuations that are "channeled" along the cold, low-speed streaks, which act as an acoustic "wave-guide." Fairly large turbulent Mach numbers and r.m.s. density fluctuations are found in both flows, especially near the walls (figures 7 & 8), which might be evidence of significant dilational effects. However, the dilational field associated with the near-wall fluctuations is not so important as to directly increase the turbulent kinetic energy dissipation rate to any great degree. This can be seen from figure 9, which gives the ratio of the mean-square dilatation fluctuations to those of the mean-square vorticity: the ratio of dilatational-to-solenoidal homogeneous kinetic energy dissipation (Zeman 1990; Blaisdell, Mansour & Reynolds 1993;

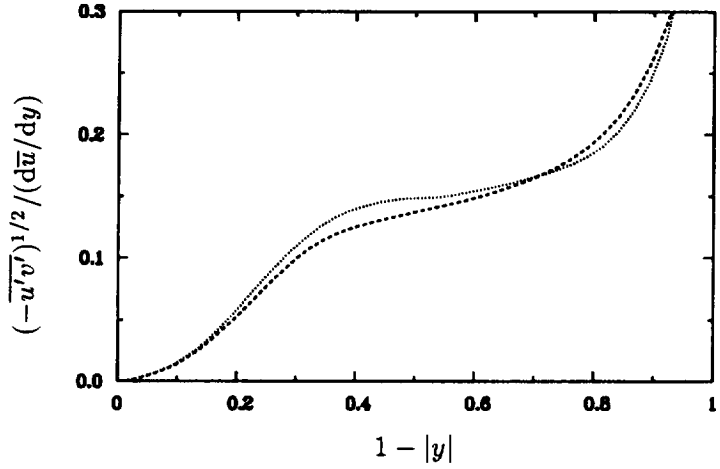

FIGURE 11. Mixing length: ----, Case A; ····· , Case B.

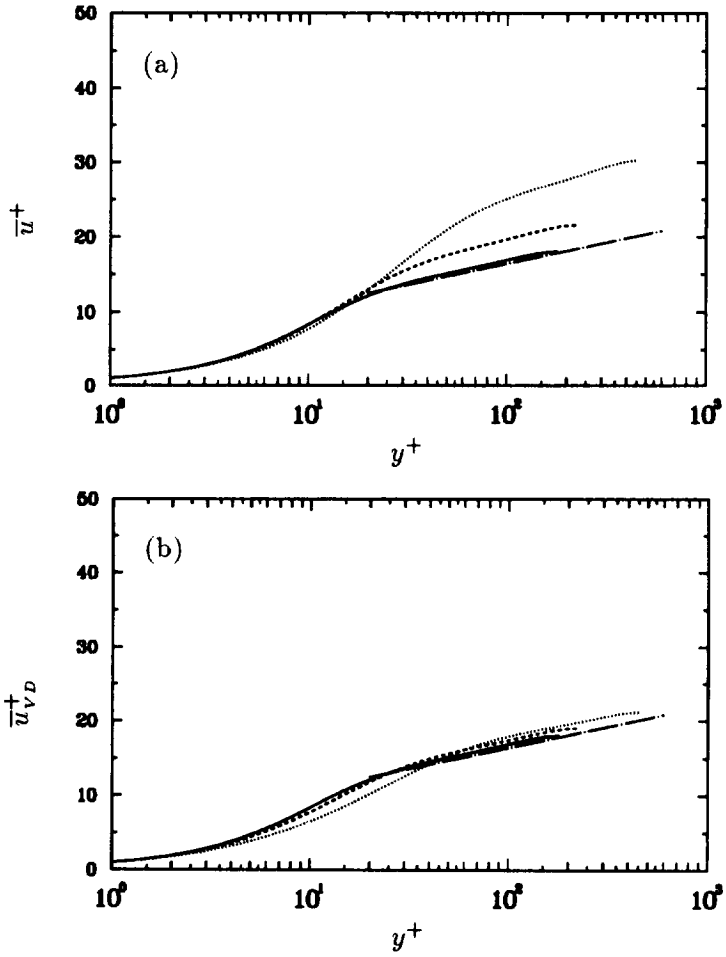

FIGURE 12. Mean velocity: (a), in wall units; (b), with Van Driest transformation; ——, $M = 0$ (Kim *et al.* 1987); ----, Case A; ····· , Case B; —·—, $2.44 \ln y^+ + 5.2$.

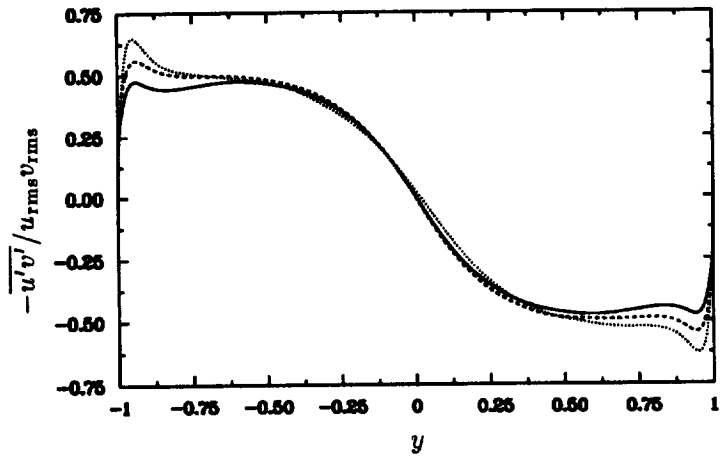

FIGURE 13. Reynolds-stress correlation coefficient: ——, $M = 0$ (Kim *et al.* 1987); ----, Case A; ····· , Case B.

Speziale & Sarkar 1991; Lele 1994). While the ratio increases by an order of magnitude as M increases from 1.5 to 3, it never becomes significantly larger than 10^{-3}. On the other hand, the pressure-dilation correlation is found to be larger than 50% of the solenoidal dissipation for *both* Mach numbers. Figure 10 shows that near the walls the dilatational field creates a strong sink of turbulent kinetic energy as kinetic energy is transferred to the pressure fluctuations (Blaisdell *et al.* 1993; Lele 1994), while toward the centerline, the pressure-dilatation acts as a smaller – but still important – *source* of kinetic energy. In the future, we hope to understand the link between the large negative $\overline{p'u'_{i,i}}$ and the observed wall-streak modification.

With such large dilational effects present, one might surmise that this flow is not governed by Morkovin's hypothesis (Favre 1992), which states that relationships between statistical properties of turbulence are unaffected by compressibility if the r.m.s. density fluctuations are small (of order 1/10) compared to the absolute density (Bradshaw & Ferriss 1971; Bradshaw 1977; Spina *et al.* 1994). But the density fluctuations for both Mach numbers are within the allowed range of $\mathcal{O}(1/10)$ (Figure 8), and for at lease one important statistical ratio, the mixing length $(-\overline{u'v'})^{1/2}/(\mathrm{d}\overline{u}/\mathrm{d}y)$, Morkovin's hypothesis is found to work fairly well. Figure 11 demonstrates that this quantity is reasonably independent of Mach number.

With the invariance of the mixing length established, the so-called Van Driest transformation for the mean velocity immediately follows. That is, the density-weighted mean velocity

$$\overline{u}^+_{VD} = \int_0^{\overline{u}^+} \left(\frac{\overline{\rho}}{\overline{\rho}_w}\right)^{1/2} \mathrm{d}\overline{u}^+ \tag{9}$$

(where $\overline{\rho}_w$ is the mean density at the wall and the + superscript denotes wall units),

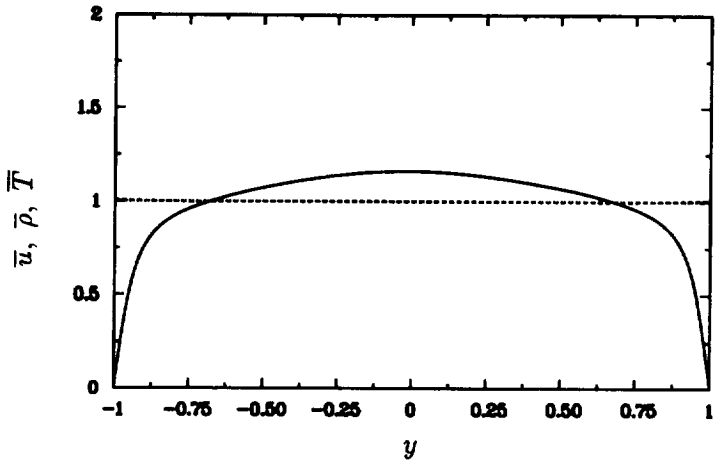

FIGURE 14. Mean profiles for Case AX: ——, $\overline{u}$; ----, $\overline{\rho}$; ····· , $\overline{T}$.

is expected to satisfy the incompressible log law,

$$\overline{u}^+_{VD} = \frac{1}{\kappa} \ln y^+ + C, \tag{10}$$

with κ and C similar to their incompressible values, $\kappa \approx 0.4$, and $C \approx 5.2$ (Bradshaw 1977; Huang, Bradshaw & Coakley 1993; Huang & Coleman 1993). The mean velocity in both wall units and the Van Driest form is plotted in figure 12 (using for the latter a mixing length formulation for the mean temperature to write $\overline{u}^+_{VD}$ as a function of $\overline{u}^+$, the surface heat flux and the mean surface temperature (Bradshaw 1977)). The agreement of the curves in figure 12b, especially their slopes, tends to reinforce the validity of the Van Driest transformation (cf. Huang & Coleman 1993) and, by extension, the Morkovin hypothesis.

Not *all* statistical ratios are found to be independent of Mach number, however, as the Reynolds-stress correlation coefficients in figure 13 show. The near-wall maximum of $|\overline{u'v'}|/u_{\rm rms}v_{\rm rms}$ increases from less then 0.5 for the incompressible channel to over 0.6 for $M = 3$. (Note that for $M = 0$, this correlation coefficient does not vary appreciably with Reynolds number (Kim *et al.* 1987), which points to compressibility and not viscous effects as the source of the differences in figure 13.)

It thus appears that the isothermal-wall channel contains some "non-Morkovin" phenomena. However, it would not at this point be appropriate to firmly state that the results in figure 13 represent a formal contradiction to the Morkovin hypothesis since the hypothesis does not (regardless of the density fluctuation level) claim to account for the influence of spatial gradients of the mean properties (Bradshaw 1977), which are apt to be important for this flow. Evidence of just how important can be found in the results from Case AX, for which $M_d = 0$ so that the mean density and temperature are constant (figure 14). The near-wall streamwise correlations for Case AX are given in figure 15. No indication of the enhanced streak coherence found for Cases A and B is observed (cf. figures 2(c) & 6(a)). Therefore, wall-normal gradients of the mean properties are required for the streak modification to

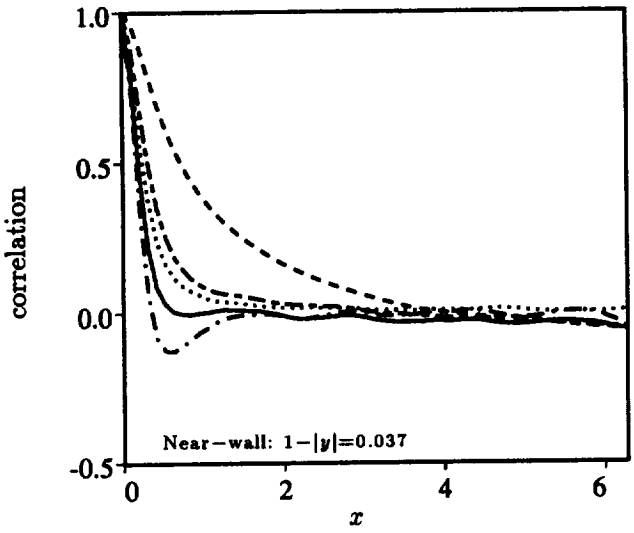

FIGURE 15. Near-wall two-point streamwise correlations for Case AX: symbols as in figure 1.

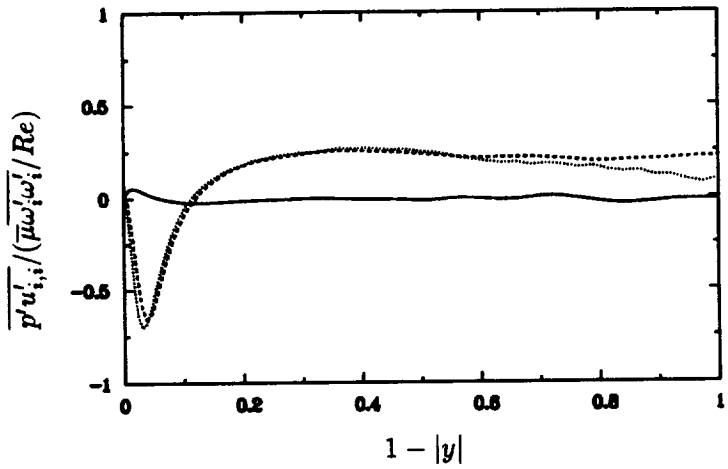

FIGURE 16. Pressure-dilatation correlation: ----, Case A; ····· , Case B; ——, Case AX.

occur. The mean gradients are also necessary for the near-wall fluctuation effects (which are presumably related to the streak coherence) to be present, as is shown by the Case AX pressure-dilatation profile in figure 16 (solid curve). Compared to the $M_d = 1.5$ and 3 results, when the mean properties are uniform, $\overline{p' u'_{i,i}}$ is much less important and represents a near-wall source rather than sink of kinetic energy.

3. Future plans

An immediate task is to attempt to resolve the open questions regarding the extra streak coherence induced by the compressibility. Namely:

A) How do the dilatation fluctuations inferred by the large pressure-dilatation correlations influence the vortical field and hence the streak structure?

B) In what sense is the enhanced streak coherence related to the increased $\overline{u'v'}$ correlation coefficient?

C) How do the variable-mean properties couple with near-wall dilatational fluctuations?

Recommended long-term efforts include comparing the present results to those computed for the adiabatic-wall channel (which to develop a statistical equilibrium will require either one wall to be isothermal or for the flow to contain a distributed heat sink). It should also be of interest to compare channel results to compressible boundary layer turbulence and thus ascertain the importance of the acoustic disturbances that are trapped between the channel walls but free to radiate away in a boundary layer. New numerical schemes, possibly using a fully implicit time-advance algorithm, should be developed to allow study of turbulent compressible flows in the hypersonic regime.

Acknowledgements

This work was done in collaboration with J. Buell, J. Kim and R. Moser. The author is also grateful to P. Bradshaw, G. Huang, S. Lele, N. Mansour, K. Shariff, A. Wray and O. Zeman for their helpful contributions. Computations were performed on the CCF and NAS computers at NASA Ames Research Center.

REFERENCES

BLAISDELL, G. A., MANSOUR, N. N., & REYNOLDS, W. C. 1993 Compressibility effects on the growth and structure of homogeneous turbulent shear flow. To appear in *J. Fluid Mech.*

BRADSHAW, P. 1977 Compressible turbulent shear layers. *Ann. Rev. Fluid Mech.* **9,** 33–54.

BRADSHAW, P. & FERRISS, D. H. 1971 Calculation of boundary layer development using the energy equation: compressible flow on adiabatic walls. *J. Fluid Mech.* **46,** 83–110.

BUELL, J. C. 1991 Direct simulations of compressible wall-bounded turbulence. In *Annual Research Briefs - 1990.* Center for Turbulence Research, Stanford Univ./NASA-Ames.

COLEMAN, G. N., BUELL, J. C., KIM, J. & MOSER, R. D. 1993 Direct simulation of compressible wall-bounded turbulence. *Ninth Symposium on Turbulent Shear Flows*, Kyoto, Japan, August 16-18, 1993.

FAVRE, A.-J. 1992 Formulation of the statistical equations of turbulent flows with variable density. *Studies in Turbulence* (T.B. Gatski *et al.*, eds.) Springer.

HUANG, P. G., BRADSHAW, P. & COAKLEY, T. J. 1993 A skin friction and velocity profile family for compressible turbulent boundary layers. *AIAA J.* **31**, 1600–1604.

HUANG, P. G. & COLEMAN, G. N. 1993 On the Van Driest transformation and compressible wall-bounded flows. Submitted to *AIAA J.*

KIM, J., MOIN, P. & MOSER, R. 1987 Turbulence statistics in fully developed channel flow at low Reynolds number. *J. Fluid Mech.* **177**, 133–166.

LELE, S. K. 1994 Compressibility effects on turbulence. To appear in *Ann. Rev. Fluid Mech.* **26**.

ROBINSON, S.K. 1991 Coherent motions in the turbulent boundary layer. *Ann. Rev. Fluid Mech.* **23**, 601–639.

SPEZIALE, C. G. & SARKAR, S. 1991 Second-order closure models for supersonic turbulent flows. *AIAA Paper No. 91-0212.*

SPINA, E.F., SMITS A.J. & ROBINSON, S.K. 1994 The physics of supersonic turbulent boundary layers. To appear in *Ann. Rev. Fluid Mech.* **26**.

TRITTON, D.J. 1961 Notes on approximations for turbulent flows with large temperature differences. *J. Fluid Mech.* **11**, 440–446.

ZEMAN, O. 1990 Dilatation dissipation: The concept and modeling in modeling compressible mixing layers. *Phys. Fluids. A.* **2**, 178–188